www.springer.com/41230
https://doi.org/10.1007/s41230-022-1234-8
Research & Development
Vol. 19 No. 4 July 2022
CHINA FOUNDRY

Effect of nitrogen on micro-pores in DD33 single crystal superalloy during solidification and homogenization

Xiang-wei Li[1], Chen Wang[1], You-zhao Zhang[1], Yu-mei Zhong[1], Li Wang[2], and *Shu-yan Zhang[1]

1. Centre of Excellence for Advanced Materials, Dongguan 523808, Guangdong, China

2. Superalloys Division, Institute of Metal Research, Chinese Academy of Sciences, Shenyang 110016, China

Abstract: The DD33 superalloy with ultra-low nitrogen (N) content was prepared by vacuum induced melting, and the effect of N on micro-pores in the DD33 single crystal nickel-base superalloy during solidification and homogenization was investigated by in-situ X-ray computed tomography (XCT). Results indicate that the volume fraction of micro-pores, including shrinkage pores and gas pores, increases from 0.08% to 0.11% with increasing N content from 5 ppm to 45 ppm during solidification. Correspondingly, the level of micro-pores in the sample with high N content is higher than that in the sample with low N content during homogenization at 1,330 °C for different time periods. However, the evolution behaviors of gas pores is different from that of shrinkage pores during solidification and homogenization. The number of gas pores is obviously larger in the high N sample during solidification, while the number of shrinkage pores and gas pores is almost the same in both samples after 1 h homogenization. Quantitative results show that the annihilation of micro-pores is associated with bubble diffusion, while the growth behavior of micro-pores during further exposure is dominated by Kirkendall-Frenkel effect.

Keywords: superalloys; solidification; micro-pores; nitrogen; X-ray computed tomography

CLC numbers: TG146.1+5 **Document code:** A **Article ID:** 1672-6421(2022)04-281-07

1 Introduction

Single crystal (SX) nickel-base superalloys have been widely used in advanced turbine blades for their high temperature capabilities. However, casting defects, such as stray grains, freckles and porosity, often occur which deteriorate the performance of the SX superalloy blades [1-3]. Although the volume fraction of porosity can be reduced effectively during directional solidification (DS), unfortunately, micro-pores are found in the interdendritic region during DS and have a negative effect on mechanical properties [4-6].

Two kinds of micro-pores, solidification pores (S-pores) formed during DS [7-9] and homogenization pores (H-pores) formed during homogenization [10-12], are observed in the interdendritic region. The formation of S-pores is due to the contraction of liquid metal and a sudden decrease in gas solubility during solidification. It was reported that the level of S-pores is affected by solidification parameters and alloying compositions [7-9]. Many studies [13-15] also suggested that S-pores have a close relationship with the nitrogen (N) content. However, the role of N in the formation of S-pores is complex, and conflicting research results have been observed so far [16-18]. In fact, shrinkage and gas pores coexist in the interdendritic region, and it is difficult to discriminate them in traditional methods. Therefore, the affecting mechanism of the N on these pores is still unclear.

In addition, the experimental superalloys used in the previous works are confined to cast and wrought polycrystalline superalloys containing different amounts of Ti elements [19-22]. Ti(C, N) carbonitrides form due to low solubility of N in the superalloys during solidification, which affect the formation of MC carbides and S-pores [16, 23, 24]. Therefore, to eliminate the influence of Ti(C, N) on micro-pores, SX superalloys without Ti elements were employed in the present study. Moreover, growth of porosity at high temperatures has been observed by many researchers [10-12]. However, the influence of N on the H-pores during homogenization, which should be influenced by homogenization temperature and time, is still less clear.

***Shu-yan Zhang**

Ph. D, Professor. Her research interest mainly focuses on the residual stress and micro mechanical properties of engineering materials using neutron and X-ray diffraction.

E-mail: shuyan.zhang@ceamat.com

Received: 2021-12-26; Accepted: 2022-06-01

In general, the content of N in the SX superalloys is about 10 ppm. To investigate the effects of N content on the micro-pore of the DD33 superalloy, two groups of the DD33 superalloys without Ti, but with ultra-low N content (5 ppm) and ultra-high N content (45 ppm) were prepared. The effects of N content on the S-pores and H-pores in the DD33 superalloy with great different N contents during solidification and homogenization were investigated. X-ray computed tomography (XCT) was used to characterize the three-dimensional (3D) information of micro-pores.

2 Experimental procedure

A 10 kg ingot of the DD33 superalloy with ultra-low N content was prepared by vacuum induced melting (VIM) and its nominal chemical compositions are given in Table 1. The ingot was divided into two parts, the first part was re-melted and directionally solidified into SX bars (Φ16 mm×200 mm) by rapid solidification processing (HRS), while the second part was re-melted with the addition of high-purity CrN and solidified under the same solidification processing parameters. The N content in the two groups of SX bars was 5 and 45 ppm, respectively.

Sample A (5 ppm N) and Sample B (45 ppm N) with 10 mm in length and 1 mm×1 mm in cross section were machined from the same position of as-cast SX bars with different N contents.

Table 1: Nominal compositions of experimental alloy (mass%)

Cr	Co	W	Mo	Re	Al	Ta	Hf	C	Ni
2.5	9	6	1.5	4	6	8	0.1	0.01	Bal.

The 3D information of micro-pores, such as the morphology, volume fraction ($V_f = \pi D^2/6$), equivalent spherical diameter (D) and surface area, was investigated by X-ray computed tomography (XCT). To characterize shrinkage pores and gas pores effectively, sphericity (S) was defined as the ratio of the surface area of the equivalent sphere (πD^2) to the surface area of the micro-pore [25].

To quantitatively analyze the effect of N on the H-pores during solution heat treatment, Samples A and B were then exposed at 1,330 °C for 1 h and 16 h in vacuum, respectively. XCT with a 160 kV X-ray source and approximately 2 μm resolution was used to in-situ characterize the 3D information of micro-pores during solidification and homogenization [26]. Microstructures of the as-cast and heat-treated samples were observed by an optical microscope (OM) and a scanning electron microscope (SEM). The area (volume) fractions of γ/γ′ eutectics were measured by OM images, and five different regions were averaged.

3 Results

3.1 As-cast microstructures

Figure 1 shows the OM images of the as-cast microstructures of the DD33 SX superalloy with different N contents. The microstructures of dendrites, including the white γ/γ′ eutectic islands in the interdendritic regions are observed. The average primary dendritic arm spacing in Sample A and Sample B is 362 μm and 342 μm, respectively. With increasing the N content from 5 ppm to 45 ppm, the volume fraction of γ/γ′ eutectics decreases from 6.6% to 3.7%, as shown in Figs. 1(c) and (d).

Figure 2 shows the SEM images of the as-cast microstructures of the DD33 SX superalloy with different N contents. Similarly, γ/γ′ eutectic islands and micro-pores in both samples

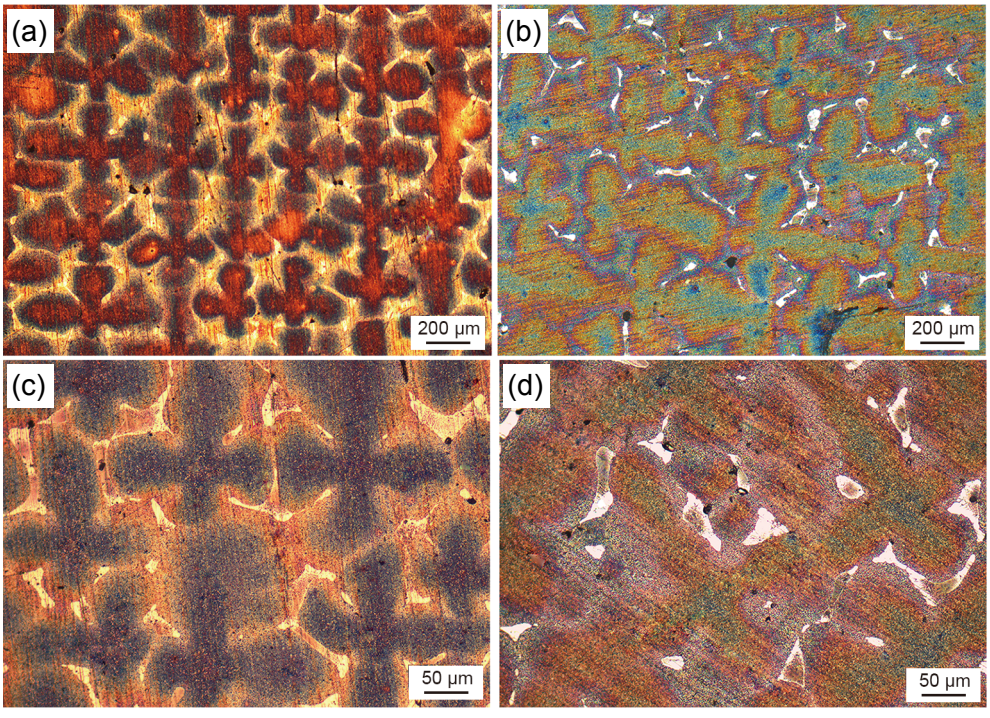

Fig. 1: OM microstructures in as-cast SX: (a, c) Sample A; (b, d) Sample B

are observed [Figs. 2(a) and (b)]. In addition, no Ti(C, N) carbonitrides are observed in Sample B with high N content. The size and volume fraction of γ′ at the dendrite core regions in Sample A and Sample B are similar [Figs. 2(c) and (d)].

3.2 Micro-pores during solidification

The 3D morphology of S-pores obtained by XCT in as-cast Samples A and B is shown in Fig. 3. The number and size of S-pores in Sample B are greater than those in Sample A. Statistic results reveal that the volume fraction of S-pores increases from 0.08% to 0.11% with increasing N content (Table 2). The average equivalent spherical diameter (D_{ave}) of S-pores increases from 11.9 μm to 12.4 μm, and the maximum size of S-pores increases from 58.7 μm to 61.1 μm.

Figure 4 shows the size distribution of micro-pores in as-cast Samples A and B. The number of both smaller S-pores (about 5 μm) and larger S-pores (>48 μm) in Sample B with a higher N content is more than that in Sample A.

Further observation reveals that there are two kinds of micro-pores based on the 3D morphology (Fig. 5): shrinkage pores with complex shapes and smaller high density round gas pores. Semi-quantitative characterization of S-pores morphology by sphericity (S) calculation for Sample A (Fig. 5) indicates that sphericity of S-pores with complex shapes is smaller than 0.9,

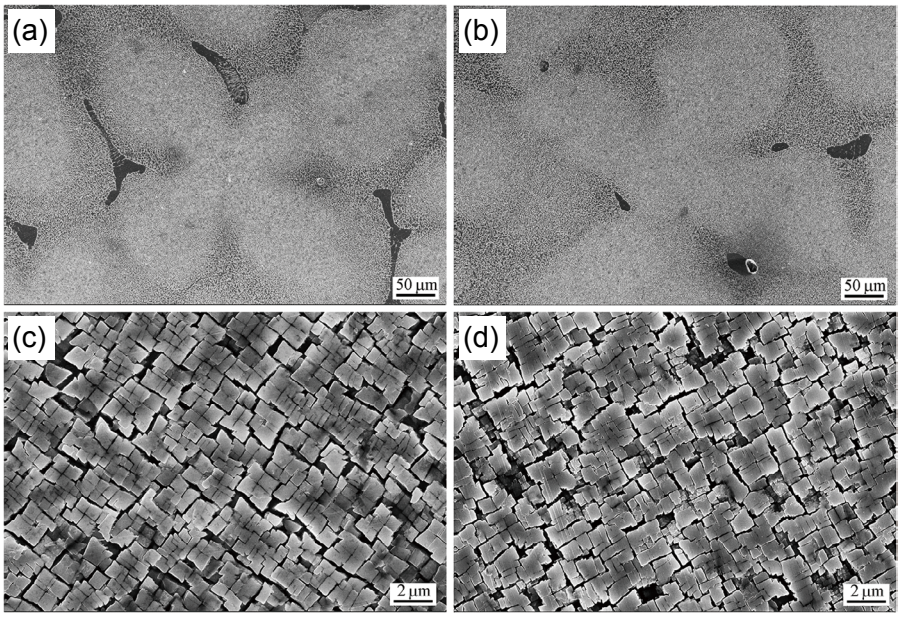

Fig. 2: SEM microstructures in as-cast SX: (a, c) Sample A; (b, d) Sample B

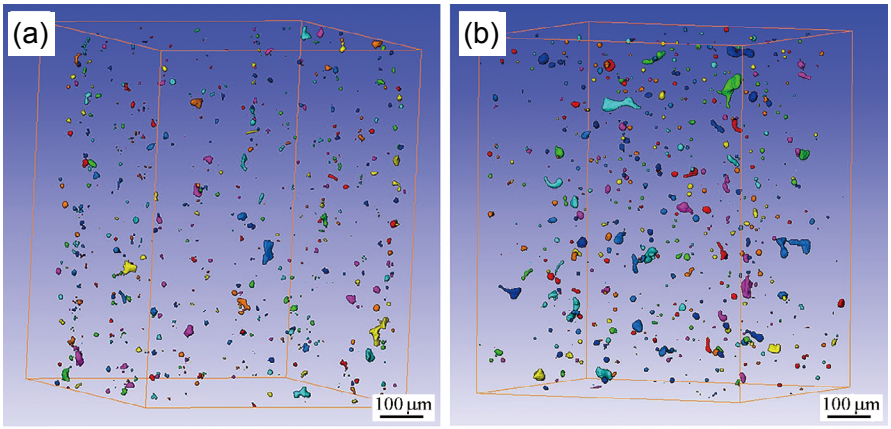

Fig. 3: 3D morphology of S-pores in as-cast SX: (a) Sample A; (b) Sample B

Table 2: Volume fraction (V_f), number (N), average diameter (D_{ave}) and the maximum size (D_{max}) of S-pores in as-cast samples with different N contents

Sample	V_f	N	D_{ave}	D_{max}
Sample A	0.08%	469	11.9 μm	58.7 μm
Sample B	0.11%	486	12.4 μm	61.1 μm

while that of round S-pores is greater than 0.9. Therefore, shrinkage (S<0.9) and gas pores (S>0.9) are defined based on the sphericity of S-pores. Statistic results reveal that the number of shrinkage pores (S<0.9) in Sample A is far smaller than that of gas pores (S>0.9), but the volume fraction of shrinkage pores (0.055%) is higher than that of gas pores (0.026%) for the alloy with 5 ppm N, as shown in Table 3.

As can be seen in Table 3, the volume fraction of shrinkage pores in Sample B (0.069%) is higher than that in Sample A with low N content (0.055%). Correspondingly, the volume fraction of gas pores in Sample B with high N content (0.041%) is higher than that in Sample A (0.026%). Similar results are observed in the number of shrinkage and gas pores. Interestingly, the average diameter of shrinkage pores is greater in Sample B, while average diameter of gas pores is greater in Sample A.

3.3 Micro-pores during homogenization

Figure 6 shows the 3D morphology of S-pores after homogenization at 1,330 °C for different times. Compared to the as-cast samples (Fig. 3), the number and size of micro-pores in heat treated samples decrease firstly during homogenization at 1,330 °C for 1 h [Figs. 6(a) and (b)], and then increase after homogenization at 1,330 °C for 16 h [Figs. 6(c) and (d)].

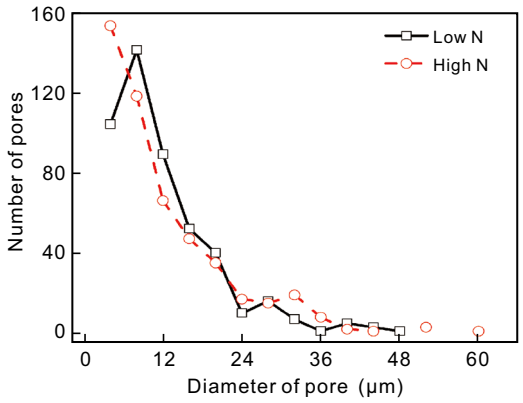

Fig. 4: Comparison of size distribution of S-pores in Sample A and Sample B with different N contents

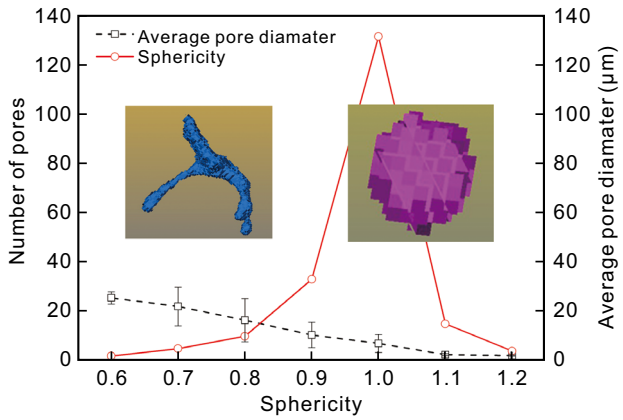

Fig. 5: Distribution of sphericity and average diameter of S-pores in as-cast Sample A

Further statistic results show that the volume fraction of pores in both samples after 1 h homogenization at 1,330 °C increases from 0.05% to 0.09% with increasing N content from 5 ppm to 45 ppm (Table 4). The number of micro-pores increases from 255 to 265. Similarly, the volume fraction of micro-pores in the samples after homogenization at 1,330 °C for 16 h increases from 0.09% to 0.15% with increasing N content, but the number of pores decreases from 696 to 639.

Figure 7 shows the size distribution of micro-pores in heat treated Samples A and B. It can be seen that the size and number of the maximum pores in Sample B after homogenization for 1 h are larger than those in Sample A [Fig. 7(a)]. After homogenization for 16 h, a reduction in the number of small size pores (about 12 μm) in Sample B with high N content is observed [Fig. 7(b)].

The volume fraction (V_f), number (N) and average diameter (D_{ave}) of gas pores (S>0.9) and shrinkage pores (S<0.9) in both samples after homogenization at 1,330 °C for different times are listed in Table 5. The volume fraction of shrinkage pores in Sample B (0.061%) is higher than that in the Sample A (0.035%). However, fewer shrinkage pores in Sample B with high N content (58) than that in the Sample A (61) are detected, especially after 16 h homogenization at 1,330 °C. Correspondingly, the volume fraction of gas pores in Sample B after 1 h homogenization (0.032%) is higher than that in Sample A (0.012%). Similar results are observed in the number of shrinkage and gas pores.

In addition, the volume fraction of pores in Sample A and Sample B decreases after 1 h homogenization. After 16 h homogenization, the average diameter of shrinkage pores in Sample A decreases from 21.56 μm to 17.07 μm (Tables 3 and 5), while that in Sample B increases from 23.03 μm to 23.89 μm. The different evolution of the average diameter of gas pores in Samples A and B is observed.

4 Discussion

It is well known that solidification initiates with freezing of primary γ dendrites, continues with the precipitation of γ/γ′ eutectic in the interdendritic region and terminates with formation of S-pores during the final stage of solidification (Fig. 1). The γ/γ′ eutectics are rich in the Al and Ti elements, and the formation of eutectics is strongly related to the microsegregation. With the nitrogen content increasing from 5 ppm to 45 ppm,

Table 3: Volume fraction (V_f), number (N) and average diameter (D_{ave}) of shrinkage pores and gas pores in as-cast samples with different N contents

Sample	Shrinkage pores (S<0.9)			Gas pores (S>0.9)		
	V_f	N	D_{ave}	V_f	N	D_{ave}
Sample A	0.055%	85	21.56 μm	0.026%	384	9.79 μm
Sample B	0.069%	87	23.03 μm	0.041%	398	9.64 μm

the microsegregation in the residual liquid decreases markedly [16], which may results in the decreasing of volume fraction of γ/γ′ eutectic. This decrease might be attributed to dendrite refinement [13].

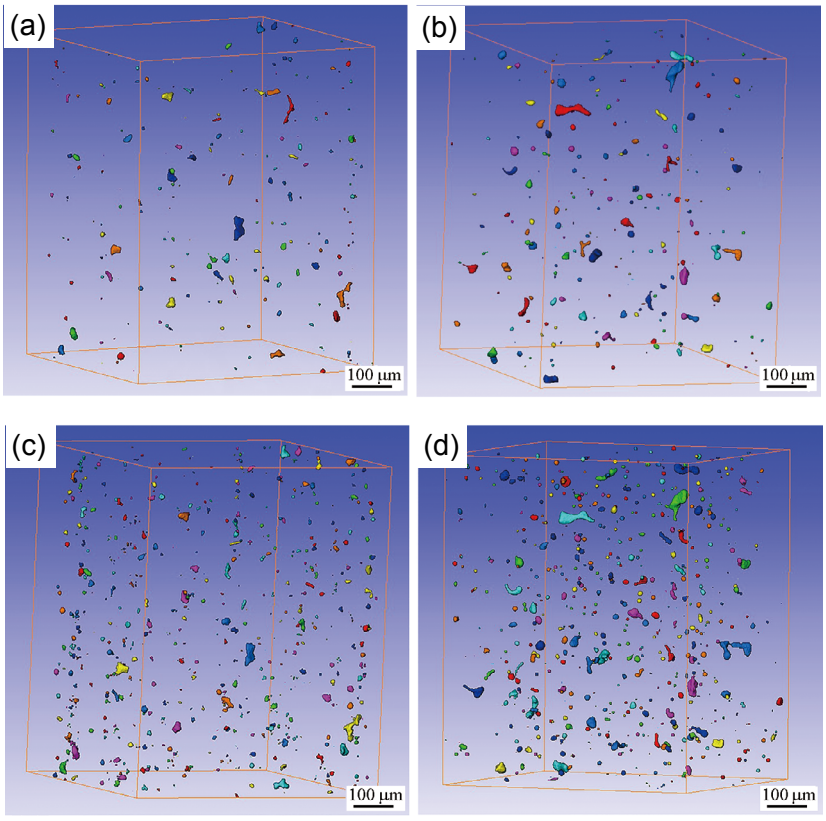

Fig. 6: 3D morphology of micro-pores in SX for Sample A (a, c) and Sample B (b, d) after homogenization at 1,330 °C for 1 h (a, b) and 16 h (c, d)

The gas elements, such as O and N, may accumulate in residual liquid in the interdendritic region. The S-pores form due to the sudden decrease in gas solubility with the precipitation of γ/γ′ eutectic during DS [26-28]. Considering the thermodynamics of nucleation of gas bubble [Eq. (1)] [29], the pressure (P_i) in the interior of the bubble is higher in Sample B with high N content. Therefore, the gas bubbles tend to form, which results in the increase of gas pores (Fig. 3) in number and volume fraction.

$$\Delta G = \alpha A + P_e - P_i \quad (1)$$

where ΔG is the total work of bubble nucleation, α is the interfacial energy per unit area, A is the new area of liquid/gas interface, P_e is the local pressure in the liquid.

In addition, Bhuiyan [30] revealed that micro-porosity is the predominant gas trap site in aluminum alloys. The higher pressure in the gas bubble may prevent contraction of liquid metal, and therefore, the average diameter of shrinkage pores is greater in Sample B (Table 3). While, the high level of micro-pores in the Sample B is associated with the decreasing of volume fraction of γ/γ′ eutectic.

During homogenization at 1,330 °C, the alloying elements, such as Al, Ta, diffuse from interdendritic regions to dendritic

Table 4: Volume fraction (V_f), number (N) and average diameter (D_{ave}) of pores in samples with different N contents after homogenization at 1,330 °C for different times

Sample	1 h			16 h		
	V_f	N	D_{ave}	V_f	N	D_{ave}
Sample A	0.05%	255	12.2 μm	0.09%	696	11.4 μm
Sample B	0.09%	265	15.4 μm	0.15%	639	14.7 μm

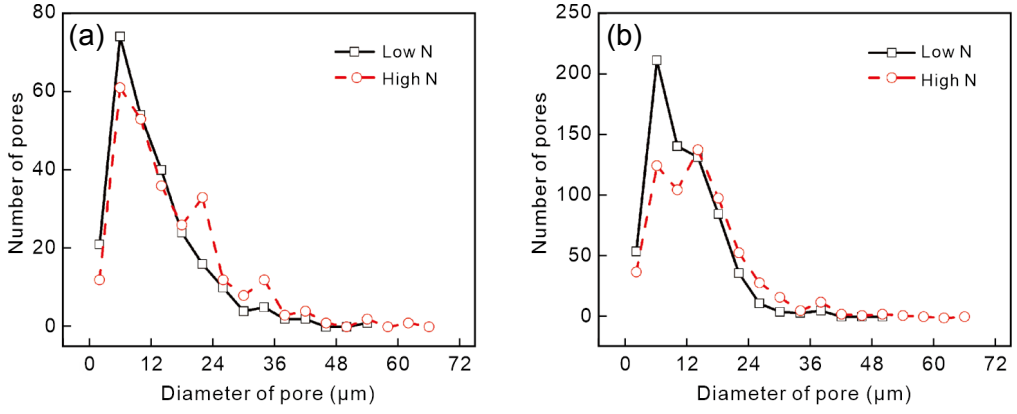

Fig. 7: Size distribution of pores in Sample A and Sample B after homogenization at 1,330 °C for 1 h (a) and 16 h (b)

Table 5: Volume fraction (V_f), number (N) and average diameter (D_{ave}) of gas pores (S>0.9) and shrinkage pores (S<0.9) in samples after homogenization at 1,330 °C for different times

Samples	Homogenization time	Shrinkage pores (S<0.9)			Gas pores (S>0.9)		
		V_f	N	D_{ave}	V_f	N	D_{ave}
Sample A	1 h	0.035%	61	20.86 μm	0.012%	194	9.56 μm
Sample B	1 h	0.061%	58	25.81 μm	0.032%	207	12.41 μm
Sample A	16 h	0.066%	222	17.07 μm	0.023%	474	8.75 μm
Sample B	16 h	0.103%	113	23.89 μm	0.072%	526	12.59 μm

cores, while alloying elements in the dendritic cores, such as Re, W, diffuse to the interdendritic regions correspondently. Therefore, the Kirkendall-Frenkel effect occurs because of the different diffusivities of the alloying elements. The imbalanced cross-diffusion flux results in an increase of vacancies in the interdendritic regions [10, 12]. Therefore, the vacancies may lead to condensation on pre-existing S-pores. Metsue and Tanguy [31, 32] found gas-vacancy clusters form in Ni by first-principles calculations. The combination of gas atoms with the vacancies may play a significant role in bubble nucleation [33, 34]. Considering the effect of thin sample surface, gas bubble can diffuse out of samples [35, 36]. The annihilation of S-pores may be related to the surface diffusion. Thus, the breakaway time of bubble [35], t_b, can be defined as:

$$t_b = K(x\%)\exp(7.5\times10^{-4}\cdot T_m / kT) \quad (2)$$

where $K(x\%)$ is a constant for a given 0.001% gas concentration, is about 0.1 [35], T_m is the melting temperature of the experimental alloy DD33, is about 1,490 °C, T is the heat treatment temperature, 1,330 °C in this study. k is Boltzmann constant. The breakaway time t_b calculated by Eq. (2) is about 10^3–10^4 s, which is fitting to the experimental results. The volume fraction of S-pores decreases in both Samples A and B after exposure at 1,330 °C for 1 h (3.6×10^3 s), as illustrated in Fig. 6. Especially, most of gas-pores quickly disappear after 1 h homogenization (Tables 4 and 5).

With extension of homogenization time, vacancy concentration continues to increase in the interdendritic regions for the imbalanced cross-diffusion flux. The vacancy supersaturation continues to condense preferentially on the S-pores, which may explain the increase of the number and volume fraction of S-pores. In addition, the vacancy supersaturation also contributes to the formation of H-pores in the interdendritic regions (Table 5). The size of micro-pores increases with the extension of homogenization time.

The gas-vacancy clusters in Sample B with high N content would accelerate the imbalanced cross-diffusion flux, and more vacancy supersaturation will condense on the S-pores and result in the increase of volume fraction of micro-pores in Sample B after 16 h homogenization (Table 4). In addition, the combination of gas-vacancy clusters with the H-pores may play a significant role in bubble nucleation, more gas bubbles can diffuse out of samples with extension of homogenization time, which decrease the number of small size pores (about 12 μm), as illustrated in Fig. 7(b).

5 Conclusions

The evolution of micro-pores in the single crystal superalloy with different N contents during solidification and homogenization was investigated. It can be concluded as follows:

(1) Two types of S-pores, shrinkage pores and gas pores, are observed in as-cast samples. The volume fraction of S-pores increases from 0.08% to 0.11% with increasing N content from 5 ppm to 45 ppm. However, the number of gas pores and the average size of shrinkage pores are larger in the sample with high N content.

(2) The volume fraction of S-pores decreases after 1 h homogenization at 1,330 °C, and the number of shrinkage pores and gas pores in both samples is almost the same. However, the average size of shrinkage pores and gas pores is larger in the sample with high N content.

(3) The volume fraction of micro-pores in both samples increases greatly after 16 h homogenization. Although the number of small micro-pores decreases, growth of shrinkage pores is observed, which results in the larger volume fraction of micro-pores in the sample containing high N.

(4) Annihilation behavior of S-pores may be related to gas bubble formation by the coexisting gas atoms and vacancies. The gas-vacancy clusters would accelerate the imbalanced cross-diffusion flux, and result in larger volume fraction of micro-pores after 16 h homogenization.

Acknowledgements

This work was financially supported by the Guangdong Major Project of Basic and Applied Basic Research (No. 2020B0301030001) and the Program for Guangdong Introducing Innovative and Entrepreneurial Teams (No. 2016ZT06G025).

References

[1] Pollock T M, Murphy W H. The breakdown of single-crystal solidification in high refractory nickel-base alloys. Metallurgical and Materials Transactions A, 1996, 27: 1081–1094.
[2] Auburtin P, Wang T, Cockcroft S L, et al. Freckle formation and freckle criterion in superalloy castings. Metallurgical and Materials Transactions B, 2000, 31: 801–811.
[3] Aveson J W. On the origin of sliver defects in single crystal investment castings. Acta Materialia, 2013, 61: 5162–5171.
[4] Li X W, Wang L, Dong J S, et al. Evolution of micro-pores in a single crystal nickel-based superalloy during solution heat treatment. Metallurgical and Materials Transactions A, 2017, 48(6): 2682–2686.
[5] Le Graverend J B, Cormier J, Kruch S, et al. Microstructural parameters controlling high-temperature creep life of the nickel-base single-crystal superalloy MC2. Metallurgical and Materials Transactions A, 2012, 43(11): 3988–3997.
[6] Lamm M, Singer R F. The effect of casting conditions on the high-cycle fatigue properties of the single crystal nickel-base superalloy PWA 1483. Metallurgical and Materials Transactions A, 2007, 38(6): 1177–1183.
[7] Uludağ M. Influence of Al-B grain refiner on porosity formation of directionally solidified Al-Si alloys. China Foundry, 2020, 17(5): 372–377.
[8] Whitesell H S, Oerfelt R A. Influence of solidification variables on the microstructure, macrosegregation, and porosity of directionally solidified Mar-M247. Materials Science and Engineering A, 2001, 318: 264–276.
[9] Luo L, Xiao C B, Chen J Y, et al. Effect of directional solidification process on microstructure and stress rupture property of a hot corrosion resistant single crystal superalloy. China Foundry, 2019, 16(1): 8–13.
[10] Anton D L, Giamei A F. Porosity distribution and growth during homogenization in single crystals of a nickel-base superalloy. Materials Science and Engineering: A, 1985, 76(1): 173–180.
[11] Bokstein B S, Epishin A I, Link T, et al. Model for the porosity growth in single-crystal nickel-base superalloys during homogenization. Scripta Materialia, 2007, 57: 801–804.
[12] Epishin A I. Diffusion processes in multicomponent nickel-base superalloy-nickel system. The Physics of Metals and Metallography, 2014, 115: 21–29.
[13] Huang X B, Zhang Y, Hu Z Q. Effect of small amounts of nitrogen on properties of a Ni-based superalloy. Materials Transactions A, 1999, 30: 1755–1761.
[14] Durber G L R, Osgerby S, Quested P N. Effect of small amounts of nitrogen and silicon on microstructure and properties of MAR-M002 nickel-base superalloy. Metals Technology, 1984, 11: 129–137.
[15] Guo X L, Yu J B, Li X F, et al. Effect of nitrogen content on the microstructure and mechanical properties of a cast nickel-base superalloy. Ironmaking & Steelmaking, 2016, 45(2): 1–9.
[16] Yuan C, Guo J T, Zhou L Z. Effect of nitrogen on microstructure and properties of a cast cobalt-base superalloy. Advanced Materials Research, 2011, 278: 472–478.
[17] Kablov D E, Chabina E B, Sidorov V V, et al. A study of the effect of nitrogen on the structure and properties of single crystals of castable refractory alloy ZhS30-VI. Metal Science and Heat Treatment, 2013, 55(7–8): 399–402.
[18] Gong L, Chen B, Yang Y Q, et al. Effect of N content on microsegregation, microstructure and mechanical property of cast Ni-base superalloy K417G. Materials Science & Engineering A, 2017, 701: 111–119.
[19] Wang L N, Zheng Q, Sun X F, et al. Oxygen and nitrogen effects on MC carbide in K465 nickel-base superalloy. Rare Metal Materials and Engineering, 2009, 38: 13–16.
[20] Yuan C, Guo J T, Li G S, et al. Effect mechanism and control of nitrogen in cast superalloys. The Chinese Journal of Nonferrous Metals, 2011, 21: 734–746.
[21] Nabavi B, Goodarzi M, Amani V. Nitrogen effect on the microstructure and mechanical properties of nickel alloys. Welding Journal, 2015, 94(2): 53–60.
[22] Ma Y C, Li S, Hao X C, et al. Research on the carbide precipitation and chromium depletion in the grain boundary of alloy 690 containing different contents of nitrogen. Acta Metallurgica Sinica, 2016, 8: 980–986. (In Chinese)
[23] Qian K, Chen B, Shu L, et al. Nitrogen solubility in liquid Ni-V, Ni-Ta, Ni-Cr-V, and Ni-Cr-Ta alloys. Metals, 2019, 1184: 9–26.
[24] Huang X B, Zhang Y, Hu Z Q. Effect of small amount of nitrogen on carbide characteristics in unidirectional Ni-base superalloy. Metallurgical and Materials Transactions A, 1997, 28: 2143–2147.
[25] Toda H. Growth behavior of hydrogen micropores in aluminum alloys during high-temperature exposure. Acta Materialia, 2009, 57(7): 2277–2290.
[26] Wang C T, Yao J, Zhao H D, et al. Influence of intensification pressures on pores in die-cast ADC12 alloys. China Foundry, 2019, 16(3): 184–189.
[27] Gupta C, Toda H, Fujioka T. Micro-pore development phenomenon in hydrogen pre-charged aluminum alloy studied using synchrotron X-ray micro-tomography. Applied Physics Letters, 2013, 103(17): 1902–1904.
[28] Cai Y, Lu T, Ma G D, et al. Effects of geometrical characteristics on defect distributions in alloy components produced by selective laser melting. China Foundry, 2021, 18(4): 369–378.
[29] Campbell J. Castings: The new metallurgy of cast metals (Second edition). Oxford: Butterworth-Heinemann, 2003.
[30] Bhuiyan M S. Combined micro-tomography and thermal desorption spectroscopy, X-ray diffraction study of hydrogen trapping behavior in 7XXX aluminum alloys. Materials Science Engineering A, 2016, 655: 221–228.
[31] Metsue A, Oudriss A, Feaugas X. Hydrogen solubility and vacancy concentration in nickel single crystals at thermal equilibrium: New insights from statistical mechanics and Ab initio calculations. Journal of Alloys and Compounds, 2016, 656: 555–567.
[32] Tanguy D, Wang Y, Connetable D. Stability of vacancy-hydrogen clusters in nickel from first-principles calculations. Acta Materialia, 2014, 78: 135–143.
[33] Raineri V, Coffa S. He-vacancy interactions in Si and their influence on bubble formation and evolution. Physical Review B, 2000, 61: 937–945.
[34] Trinkaus H, Singh B N. Helium accumulation in metals during irradiation – where do we stand? Journal of Nuclear Materials, 2003, 323: 229–242.
[35] Evans J H. Breakaway bubble growth during the annealing of helium bubbles in metals. Journal of Nuclear Materials, 2004, 334: 40–46.
[36] Zhang B L, Wang J, Li M, et al. A molecular dynamics study of helium bubble formation and gas release near titanium surfaces. Journal of Nuclear Materials, 2013, 438: 178–182.